High-throughput calculations of spin Hall conductivity in non-magnetic 2D materials

Jiaqi Zhou,^{1,*} Samuel Poncé,^{2,3,†} and Jean-Christophe Charlier^{1,‡}

¹Institute of Condensed Matter and Nanosciences,
Université catholique de Louvain, 1348 Louvain-la-Neuve, Belgium

²European Theoretical Spectroscopy Facility and
Institute of Condensed Matter and Nanosciences,
Université catholique de Louvain, 1348 Louvain-la-Neuve, Belgium

³WEL Research Institute, Avenue Pasteur 6, 1300 Wavre, Belgium

(Dated: January 7, 2025)

Abstract

Spin Hall effect (SHE) in two-dimensional (2D) materials is promising to effectively manipulate spin angular momentum and identify topological properties. In this work, we implemented an automated Wannierization with spin-orbit coupling on 426 non-magnetic monolayers including 210 metal and 216 insulators. Intrinsic spin Hall conductivity (SHC) has been calculated to find candidates exhibiting novel properties. We discover that $Y_2C_2I_2$ has an unconventional SHE with canted spin due to low crystal symmetry, Ta_4Se_2 is a metallic monolayer with exceptionally high SHC, and the semi-metal Y_2Br_2 possesses efficient charge-to-spin conversion induced by anti-crossing in bands. Moreover, quantum spin Hall insulators are investigated for quantized SHC. The present work provides a high-quality Wannier Hamiltonian database of 2D materials, and paves the way for the integration of 2D materials into high-performance and low-power-consumption spintronic devices.

^{*} jiaqi.zhou@uclouvain.be

[†] samuel.ponce@uclouvain.be

[‡] jean-christophe.charlier@uclouvain.be

Spin Hall effect (SHE) is a phenomenon emerging from spin-orbit coupling (SOC) where an external electric field can induce a transverse spin current [1]. As an effective method to control spin transport, the SHE has been extensively investigated in bulk heavy metals [2]. However, simple heavy metals are constrained by symmetry and only present conventional SHE where spin current, electric field, and spin orientation are orthogonal to each other. Constrained by this strict rule, an external magnetic field is required to switch perpendicular magnetization [3], hindering device minimization. Besides, defined as the ratio of spin Hall conductivity (SHC) to charge conductivity, the spin Hall ratio (SHR) is reduced by high charge conductivity in heavy metals, leading to a low charge-to-spin conversion efficiency [2]. Van der Waals materials emerge as promising candidates to overcome these challenges. SHCs have been studied in two-dimensional (2D) transition-metal dichalcogenide (TMDC) materials [4–11]. Compared with high-symmetry bulk heavy metals, 2D materials with low-symmetry structures can induce unconventional SHEs [12, 13]. In addition, the reduced charge conductivity in 2D materials enables efficient charge-to-spin conversion [14, 15]. More importantly, the reduced dimension induces quantum spin Hall effect in topological 2D materials [16], offering robust and quantized SHCs in bandgaps of quantum spin Hall insulators (QSHIs) [17–19]. However, current researches on SHE of 2D materials are mostly limited to TMDC materials, while a large-scale study on 2D materials for spintronics is still absent.

Wannier functions [20, 21] are extensively used to study the SHC [22]. Recent works have developed frameworks for the high-throughput Wannierization. Symmetrized Wannier Hamiltonians have been generated for the strained III-V semiconductor materials by applying post-processing symmetrization [23]. In addition, the single-criterion decision-making algorithm with no need for an initial guess has been validated for band interpolations on a dataset of 200 materials [24]. Moreover, Wannier Hamiltonians including SOC for 1406 3D and 365 2D materials were generated using hydrogenic orbital projections with hints from pseudopotentials [25]. Recently, the projectability-disentangled Wannier functions have been proposed where the initial guess is given by a projectability measure for each Bloch state onto atomic orbitals [26, 27].

In this work, we perform a high-throughput study of spin Hall conductivity in non-magnetic 2D materials using density functional theory (DFT) and Wannier functions. Leveraging the scalar-relativistic MC2D database [28, 29], all the rare-earth-free monolayers with up to 6

atoms per unit cell are considered, yielding 426 exfoliable materials. These materials are investigated with *ab initio* calculations including SOC. Intrinsic SHCs are calculated in all the materials to reveal exotic SHE. Unconventional SHE is found in a low-symmetry metal, materials with high SHC values are listed, and a high SHR is found in a semi-metal. Finally, SHCs of topological insulators are studied to understand the importance of spin conservation for quantized SHC.

RESULTS AND DISCUSSIONS

To match the typical experimental setup, we focus on the SHC where the spin current is along x, the electric field is along y, and the spin orientation is along α direction. The intrinsic SHC in a weak scattering limit can be calculated by the Kubo formula [22, 30]:

$$\sigma_{xy}^{\alpha} = \frac{\hbar}{2e} \frac{e^2}{\hbar} \int_{BZ} \frac{\mathrm{d}^2 \mathbf{k}}{(2\pi)^2} \Omega_{xy}^{\alpha}(\mathbf{k}), \tag{1}$$

where BZ denotes the Brillouin zone, and the spin Berry curvature (SBC) is given as

$$\Omega_{xy}^{\alpha}(\mathbf{k}) = \sum_{n} f_{n\mathbf{k}} \Omega_{n,xy}^{\alpha}(\mathbf{k}), \tag{2}$$

$$\Omega_{n,xy}^{\alpha}(\mathbf{k}) = \hbar^2 \sum_{m \neq n} \frac{-2 \operatorname{Im}[\langle n\mathbf{k} | \hat{j}_{\alpha} | m\mathbf{k} \rangle \langle m\mathbf{k} | \hat{v}_{y} | n\mathbf{k} \rangle]}{(\varepsilon_{n\mathbf{k}} - \varepsilon_{m\mathbf{k}})^2 + \eta^2}.$$
 (3)

In the above equations, $f_{n\mathbf{k}}$ denotes the Fermi-Dirac distribution $f_{n\mathbf{k}}(\mu, T) = \frac{1}{e^{(\varepsilon_{n\mathbf{k}}-\mu)/(k_BT)}+1}$, where μ is the Fermi energy. $\hat{j}_{\alpha} = \frac{1}{2}\{\hat{\sigma}_{\alpha}\hat{v}_x + \hat{v}_x\hat{\sigma}_{\alpha}\}$ is the spin current operator, $\hat{\sigma}_{\alpha}$ is the Pauli operator, \hat{v}_x and \hat{v}_y are velocity operators, η is the broadening approximated as extrinsic scattering [31].

To compute the SHC on ultra-dense \mathbf{k} grids, we construct an *ab initio* Wannier Hamiltonian database and assess its quality by comparing the average differences between DFT bands and Wannier bands, given as [26, 27]

$$\eta_{\nu} = \sqrt{\frac{\sum_{n\mathbf{k}} \tilde{f}_{n\mathbf{k}} \left(\varepsilon_{n\mathbf{k}}^{\text{DFT}} - \varepsilon_{n\mathbf{k}}^{\text{Wan}}\right)^{2}}{\sum_{n\mathbf{k}} \tilde{f}_{n\mathbf{k}}}}$$
(4)

where ${\bf k}$ denotes eigenstates along the high-symmetry ${\bf k}$ -path of the band structure, $\tilde{f}_{n{\bf k}}=$

 $\sqrt{f_{n\mathbf{k}}^{\mathrm{DFT}}\left(\mathrm{E}_{\mathrm{F}}+\nu,\,T\right)f_{n\mathbf{k}}^{\mathrm{Wan}}\left(\mathrm{E}_{\mathrm{F}}+\nu,\,T\right)}$ where $\mathrm{E}_{\mathrm{F}}+\nu$ represents energy position, thus η_{ν} denotes the difference given by comparing $\varepsilon_{n\mathbf{k}}^{\mathrm{DFT}}$ and $\varepsilon_{n\mathbf{k}}^{\mathrm{Wan}}$ below $\mathrm{E}_{\mathrm{F}}+\nu$. Since the Wannier Hamiltonian describes the low-energy subspace, it is expected that the Wannier-interpolated bands will deviate more from the DFT results in the higher energy region. Therefore, the higher ν is, the larger η_{ν} is expected to be. The symbols η_{1} and η_{2} denote the band distance for the bands below $\mathrm{E}_{\mathrm{F}}+1$ eV and $\mathrm{E}_{\mathrm{F}}+2$ eV, respectively. For η_{1} , 98% of materials show a band distance below 10 meV, and 92% of materials show a small band distance below 2 meV. For η_{2} , 93% of materials show a distance below 10 meV, and 70% of materials show a distance below 2 meV, highlighting the overall quality of Wannier Hamiltonians in our database. η distributions are provided in Supplementary Fig. 1(b). Bands of all the metals and insulators are present in Supplementary Secs. 4 and 5.

Unconventional spin Hall effect

Neumann's principle states that symmetries of the physical property must include all symmetries of the crystal [32], indicating that a high-symmetry crystal would impose more restrictions on the allowed property. As a result, high-symmetry monolayers can only present one unique non-zero SHE component σ_{xy}^z [33], which is called conventional SHE where the spin orientation is perpendicular to the xy-plane as shown in Fig. 1(a). In contrast, low-symmetry materials can lead to unconventional SHE [33]. The unconventional SHE is important for the field-free switching of perpendicular magnetization, since it can provide a canted torque to trigger the spin dynamics without external magnetic field [34].

To discover intrinsically unconventional SHE, we focus on metals with non-zero σ_{xy}^x and σ_{xy}^y as illustrated in Fig. 1(a). A symmetry precision of 0.01 was applied in the ASE package [35] to screen materials with low-symmetry space group. After screening, we find 17 metals with low symmetry. Most of them present small SHCs. Notably, $Y_2C_2I_2$ is found to present a high σ_{xy}^x at the Fermi energy as shown in Fig. 1(b). With the C2/m space group, $Y_2C_2I_2$ only has one mirror symmetry m_y as shown in Fig. 1(c), allowing the spin current with spin orientation in xz-plane. To analyze the σ_{xy}^x and σ_{xy}^z behaviors, Fig. 1(d) presents the bands projected by SBC along the X- Γ **k**-path. The SOC results in an anti-crossing gap in $Y_2C_2I_2$. The positive and negative $\Omega_{n,xy}^x$ are perfectly separated by the Fermi energy, leading to a peak of the integral Ω_{xy}^x . In contrast, σ_{xy}^z is limited, leading to a slightly canted

spin orientation in the xz-plane. The magnitude of SBC was dealt with a logarithm function as Eq. (52) in Ref. [22] for simplicity. The dynamical stability has been validated by its phonon dispersion in Supplementary Fig. 7.

High spin Hall conductivity

Although only a few materials have unconventional SHE components, the conventional component σ_{xy}^z is allowed for all the materials. The known σ_{xy}^z values in 2D materials are limited, for instance, MoS₂ monolayer only presents $\sigma_{xy}^z \approx 0.2~e/4\pi$ with doping [36]. To find high values for σ_{xy}^z in metals, SHC calculations are performed on all 210 metals including semi-metals, where 15 materials display exceptional $|\sigma_{xy}^z| > 2~e/4\pi$, see details in Supplementary Sec. 2. Unfortunately, most of them are unstable according to phonon dispersions. Table 1 lists 3 materials whose mechanical stabilities have been validated by positive phonon dispersions, details are given in Supplementary Sec. 3.

Ta₄Se₂ monolayer presents the highest value $\sigma_{xy}^z = -3.4 \ e/4\pi$. Considering that Ta₄Se₂ is composed of heavy elements, its high SHC is attributed to strong SOC which opens up an anti-crossing band gap around Fermi energy. Figures 2(a) and 2(b) show the bands of Ta₄Se₂ projected by SBC and energy-dependent σ_{xy}^z . For $\mu = 0$, the positive and negative SBCs compete as shown in Fig. 2(c). The SHC of Ta₄Se₂ can be further enhanced by tuning the Fermi energy position. For $\mu = 0.21$ eV, the negative SBC is dominant in the whole BZ as shown in Fig. 2(d), maximizing the σ_{xy}^z amplitude to be $-12 \ e/4\pi$. This finding suggests that doping is an effective method to increase SHC in Ta₄Se₂.

Apart from Ta₄Se₂, Sn₂P and Y₂Br₂ are also found to exhibit high σ_{xy}^z values –2.7 and 2.4 $e/4\pi$, respectively. Note that the high-symmetry Sn₂P monolayer reported by the MC2D database presents imaginary phonon frequency, thus its structure was relaxed without preserving any symmetry, leading to the P1 space group. It is found that although in a broken-symmetry regime, the relaxed structure is very close to the original structure, namely, the movement of every atom is less than 10^{-3} Å. Still, this low-symmetry Sn₂P monolayer with positive phonon dispersion is employed to study SHC. Besides, the possible magnetism in Y₂Br₂ is excluded by the negligible magnetic anisotropic energy. Additional details are given in Supplementary Sec. 3.

High spin Hall ratio

The conversion efficiency from charge current to spin current via the spin Hall effect is evaluated by the spin Hall ratio, defined as $\xi = \frac{2e}{\hbar} \left| \frac{\sigma_{xy}^z}{\sigma_{xx}} \right|$ [37]. The semi-metal WTe₂ has been reported for an efficient conversion [38] since its resistive conductivity σ_{xx} is reduced by limited carrier around Fermi energy. Remarkably, Table 1 includes Y₂Br₂ which is also a semi-metal with high σ_{xy}^z . Figure 3(a) shows that Y₂Br₂ has a small energy overlap between the conduction band and the valence band. The SOC-induced anti-crossing gaps separate the negative and positive SBCs perfectly, leading to a σ_{xy}^z peak around Fermi energy as given in Fig. 3(b). The dynamical stability of Y₂Br₂ is validated by the positive phonon dispersion as shown in Fig. 3(c). Our finding suggests that Y₂Br₂ could be a promising candidate for high SHR.

Calculation of charge conductivity is required to compute the SHR in Y₂Br₂. For an intrinsic material, the electron-phonon coupling (EPC) is a fundamental interaction that affects the scattering rate, which can be accurately calculated using *ab initio* approach [39]. The phonon-limited charge conductivity σ_{xx} is given by [40]

$$\sigma_{xx} = \frac{-e}{S^{uc}} \sum_{n} \int \frac{\mathrm{d}^{2} \mathbf{k}}{\Omega^{BZ}} v_{n\mathbf{k}x} \partial_{E_{x}} f_{n\mathbf{k}}, \tag{5}$$

where $S^{\rm uc}$ is the unit cell area, $\Omega^{\rm BZ}$ is the BZ area, and $v_{n\mathbf{k}x}=\hbar^{-1}\partial\varepsilon_{n\mathbf{k}}/\partial k_x$ is the band velocity. The linear variation of the electronic occupation function $f_{n\mathbf{k}}$ in response to E_x , $\partial E_x f_{n\mathbf{k}}$, can be obtained by solving the Boltzmann transport equation [41] which induces the scattering rate given by

$$\tau_{n\mathbf{k}}^{-1} = \frac{2\pi}{\hbar} \sum_{m\nu} \int \frac{\mathrm{d}^2 \mathbf{q}}{\Omega^{\mathrm{BZ}}} |g_{mn\nu}(\mathbf{k}, \mathbf{q})|^2 \left[(n_{\mathbf{q}\nu} + 1 - f_{m\mathbf{k}+\mathbf{q}}^0) \delta(\varepsilon_{n\mathbf{k}} - \varepsilon_{m\mathbf{k}+\mathbf{q}} - \hbar\omega_{\mathbf{q}\nu}) + (n_{\mathbf{q}\nu} + f_{m\mathbf{k}+\mathbf{q}}^0) \delta(\varepsilon_{n\mathbf{k}} - \varepsilon_{m\mathbf{k}+\mathbf{q}} + \hbar\omega_{\mathbf{q}\nu}) \right], \quad (6)$$

where $g_{mn\nu}(\mathbf{k}, \mathbf{q})$ is the electron-phonon matrix element with phonon frequency $\omega_{\mathbf{q}\nu}$. The \mathbf{k} -resolved effective scattering rate, defined as $\tau_{\mathbf{k}}^{-1} = \sum_{n} \frac{-\partial f_{n\mathbf{k}}^{0}}{\partial \varepsilon_{n\mathbf{k}}} \tau_{n\mathbf{k}}^{-1}$, is given in Fig. 3(d). Strong scattering occurs around the K points where Fermi energy crosses the anti-crossing gap. The small bandgap facilitates scattering between electron states, enhancing EPC and

scattering rates. Besides, the pattern of Fig. 3(d) is determined by structural symmetry which also forces $\sigma_{xx} = \sigma_{yy}$ in Y₂Br₂.

The SHR of Y₂Br₂ can be obtained from the calculated SHC and charge conductivity. Y₂Br₂ presents an SHC of $\sigma_{xy}^z = 2.4~e/4\pi$, and a charge conductivity of $\sigma_{xx} = 6.1~e^2/h$. Defined as $\xi = \frac{2e}{\hbar} \left| \frac{\sigma_{xy}^z}{\sigma_{xx}} \right|$, the room-temperature SHR in Y₂Br₂ is calculated to be $\xi = 0.4$, much higher than SHRs ~ 0.01 in typical heavy metals [2]. Our results demonstrate that attributed to anti-crossings in semi-metal bands, Y₂Br₂ is a promising candidate for efficient charge-to-spin conversion.

Quantized spin Hall conductivity

As the last part of this work, gapped materials are investigated. It is instructive to compute the SHC of materials to discover topological insulators which possess a perfect SHC plateau inside their bandgap. A typical QSHI presents a quantized SHC with amplitude of $\sigma_{xy}^z = n \ e/2\pi$ where n is an integer [42]. However, in practice, the SHC plateau is not always well quantized; namely, some $\mathbb{Z}_2 = 1$ QSHIs manifest significant deviations from their expected quantized value [43].

To clarify the mechanism of quantized SHC, we calculated the σ_{xy}^z of 216 insulators with T=0 K and $\eta=5$ meV. We find 8 materials with SHC plateau in the bandgap. Among these materials, Bi₂, Hf₂Br₂, CuLi₂As, and Ti₂N₂I₂ have been validated as QSHIs with $\mathbb{Z}_2=1$ [16]. The other 4 materials are Li₂Tl₂, Hg₃S₂, Hg₄O₂, and In₂Bi₂ which possess soft phonon modes. Thus we only list the results of the former 4 materials in Table 2. All 4 materials present a non-zero SHC plateau inside the bandgap. However, the SHC amplitudes vary and the β -Bi₂ monolayer shows $\sigma_{xy}^z=0.5~e/2\pi$ while CuLi₂As presents a quantized SHC of $\sigma_{xy}^z=1.0~e/2\pi$.

The potentially quantized SHC can be interpreted by spin conservation. Symmetry analysis [33] illustrates that in the β -Bi₂ monolayer, SHC components of σ_{xy}^y and σ_{xy}^z are allowed while σ_{xy}^x is prohibited. Indeed, Fig. 4(a) shows non-zero σ_{xy}^y and σ_{xy}^z SHC plateaus inside bandgap. Besides, the edge-state spin of Bi₂ is neither conserved nor robust as shown in Fig. 4(c). In contrast, Fig. 4(b) shows that only σ_{xy}^z is allowed in CuLi₂As, which presents a pair of helical edge states with well-conserved S_z as shown in Fig. 4(d). As a result, we find a quantized SHC $\sigma_{xy}^z = 1.0 \ e/2\pi$ in CuLi₂As. Besides, with the same space group as Bi₂,

 Hf_2Br_2 also presents a deviation from quantized SHC due to non-zero σ_{xy}^y and non-zero S_y on edge states. $Ti_2N_2I_2$ presents similar behaviors as $CuLi_2As$. It can be concluded that the non-conserved S_z is destructive for quantized SHC. Calculations of SHC and spin-projected edge states are necessary to predict the value of SHC plateau in QSHI.

In conclusion, leveraging the MC2D database, we implemented an automated Wannierization based on orbital information from the pseudopotentials for 426 non-magnetic monolayers including 210 metals and 216 insulators. The quality of Wannierizations has been validated by comparing DFT bands with Wannier bands, and the Wannier Hamiltonians are provided to the community. Exotic spin Hall effects are discovered in diversified materials. For metals, it is found that $Y_2C_2I_2$ displays canted spin Hall effect due to its low-symmetry structure. Besides, metallic candidates with high SHC values are listed, indicating Ta_4Se_2 as the optimal candidate. Efficient charge-to-spin conversion is reported in the semi-metal Y_2Br_2 . For insulators, SHC plateaus are revealed in quantum spin Hall insulators, highlighting the importance of conserved S_z for quantized SHC. This comprehensive work enhances the understanding of spin Hall effect in 2D systems, suggesting promising materials for advanced spintronic devices. Moreover, the provided Wannier database could be further employed to explore additional spin-orbitronic phenomena.

METHODS

DFT calculations

DFT calculations were performed using the Quantum ESPRESSO package [44] within the Perdew-Burke-Ernzerhof (PBE) parametrization of generalized gradient approximation (GGA). AIIDA [45] was employed to calculate 426 non-magnetic monolayers from MC2D database [28, 29] with a **k**-mesh density of 0.15 Å⁻¹, Marzari-Vanderbilt smearing [46] of 0.01 Ry, and 2D Coulomb truncation scheme [47]. Although the SSSP library [48] was used in MC2D database, it only includes scalar-relativistic pseudopotentials. To investigate SOC effect, our work employed PSEUDODOJO library [49] which includes both scalar-relativistic and fully relativistic pseudopotentials. The fully relativistic pseudopotentials were applied to MC2D materials without relaxation. After screening out 8 candidates with superior SHC properties, the scalar-relativistic PSEUDODOJO pseudopotentials were used to relax

structures and calculate phonon dispersions. For the relaxed 8 structures, the fully relativistic PSEUDODOJO pseudopotentials were applied to the DFT calculations and Wannierizations.

Wannierizations

In our work, the initial guess for projector is given by the hydrogenic orbital with hints from Pseudodo [50]. The semicore orbitals corresponding to deep bands are excluded from projections. The maximum of the frozen window is set as Fermi energy + 2 eV (Fermi energy is the conduction band minimum for insulators) which is numerically verified to be the optimal value as shown in Supplementary Fig. 1(a). To provide a high-quality Wannier Hamiltonian database, failed cases (42/426) have been manually corrected by tuning the frozen window, increasing the number of electronic states, or modifying initial projections.

Transport calculations

The spin Hall conductivity was calculated with the WANNIER90 package [22, 51] with a fine **k**-mesh density of 0.005 Å⁻¹ for the Wannier interpolation. A Fermi-Dirac distribution function of T=300 K and a broadening of 2 meV were considered if not specified. The charge conductivity was calculated using the EPW package [52, 53]. A coarse $12 \times 12 \times 1$ **k/q**-grid was interpolated on a fine **k/q**-grid of $360 \times 360 \times 1$. The electron wavefunctions and dynamical matrices were calculated using fully and scalar relativistic pseudopotentials, respectively [54]. An adaptive smearing [55], a phonon frequency cutoff of 1 cm⁻¹ and a 300 K temperature are used. Edge states of topological insulators were calculated by WannierTools [56].

DATA AVAILABILITY

Details including electronic structures and phonon dispersions of promising materials investigated in this work, as well as fully relativistic bands of 426 monolayers, are given in the Supplementary Material. The input and output files, Wannier Hamiltonians, and bands data of promising materials and 426 monolayers are provided on Materials Cloud Archive [57].

REFERENCES

- Sinova, J., Valenzuela, S. O., Wunderlich, J., Back, C. H. & Jungwirth, T. Spin Hall effects. Rev. Mod. Phys. 87, 1213–1260 (2015).
- [2] Tao, X. et al. Self-consistent determination of spin Hall angle and spin diffusion length in Pt and Pd: The role of the interface spin loss. Sci. Adv. 4, eaat1670 (2018).
- [3] Liu, L., Lee, O. J., Gudmundsen, T. J., Ralph, D. C. & Buhrman, R. A. Current-Induced Switching of Perpendicularly Magnetized Magnetic Layers Using Spin Torque from the Spin Hall Effect. Phys. Rev. Lett. 109, 096602 (2012).
- [4] Ahn, E. C. 2D materials for spintronic devices. npj 2D Mater. Appl. 4, 1–14 (2020).
- [5] Safeer, C. K. et al. Room-Temperature Spin Hall Effect in Graphene/MoS2 van der Waals Heterostructures. Nano Lett. 19, 1074–1082 (2019).
- [6] MacNeill, D. et al. Control of spin-orbit torques through crystal symmetry in WTe₂/ferromagnet bilayers. Nat. Phys. 13, 300–305 (2017).
- [7] Shi, S. et al. All-electric magnetization switching and Dzyaloshinskii–Moriya interaction in WTe₂/ferromagnet heterostructures. Nat. Nanotechnol. 14, 945–949 (2019).
- [8] Guimarães, M. H. D., Stiehl, G. M., MacNeill, D., Reynolds, N. D. & Ralph, D. C. Spin-Orbit Torques in NbSe₂/Permalloy Bilayers. *Nano Lett.* 18, 1311–1316 (2018).
- [9] Stiehl, G. M. et al. Layer-dependent spin-orbit torques generated by the centrosymmetric transition metal dichalcogenide β MoTe₂. Phys. Rev. B **100**, 184402 (2019).
- [10] Xu, H. et al. High Spin Hall Conductivity in Large-Area Type-II Dirac Semimetal PtTe₂. Adv. Mater. 32, 2000513 (2020).
- [11] Mishra, A. et al. Preserving SOC for enhancement of spin-to-charge conversion efficiency via Cu intercalation in $MoS_2/CoFeB$ heterostructures. arXiv (2024). 2411.18582.
- [12] Zhou, J. & Charlier, J.-C. Controllable spin current in van der Waals ferromagnet Fe₃GeTe₂.
 Phys. Rev. Res. 3, L042033 (2021).
- [13] Ji, G., Zhang, Y., Chai, Y. & Nan, T. Recent progress on controlling spin-orbit torques by materials design. *npj Spintronics* **2**, 1–14 (2024).
- [14] Vila, M. et al. Low-symmetry topological materials for large charge-to-spin interconversion: The case of transition metal dichalcogenide monolayers. *Phys. Rev. Res.* **3**, 043230 (2021).

- [15] Safeer, C. K. et al. Large Multidirectional Spin-to-Charge Conversion in Low-Symmetry Semimetal MoTe₂ at Room Temperature. Nano Lett. 19, 8758–8766 (2019).
- [16] Grassano, D., Campi, D., Marrazzo, A. & Marzari, N. Complementary screening for quantum spin Hall insulators in two-dimensional exfoliable materials. *Phys. Rev. Mater.* 7, 094202 (2023).
- [17] Bai, Y. et al. Doubled quantum spin Hall effect with high-spin Chern number in α -antimonene and α -bismuthene. Phys. Rev. B 105, 195142 (2022).
- [18] Matusalem, F. et al. Quantization of spin Hall conductivity in two-dimensional topological insulators versus symmetry and spin-orbit interaction. Phys. Rev. B 100, 245430 (2019).
- [19] Matthes, L., Küfner, S., Furthmüller, J. & Bechstedt, F. Intrinsic spin Hall conductivity in one-, two-, and three-dimensional trivial and topological systems. *Phys. Rev. B* 94, 085410 (2016).
- [20] Marzari, N., Mostofi, A. A., Yates, J. R., Souza, I. & Vanderbilt, D. Maximally localized Wannier functions: Theory and applications. Rev. Mod. Phys. 84, 1419–1475 (2012).
- [21] Marrazzo, A. et al. The Wannier-Functions Software Ecosystem for Materials Simulations. arXiv (2023). 2312.10769.
- [22] Qiao, J., Zhou, J., Yuan, Z. & Zhao, W. Calculation of intrinsic spin Hall conductivity by Wannier interpolation. *Phys. Rev. B* **98**, 214402 (2018).
- [23] Gresch, D. et al. Automated construction of symmetrized Wannier-like tight-binding models from ab initio calculations. Phys. Rev. Mater. 2, 103805 (2018).
- [24] Vitale, V. et al. Automated high-throughput Wannierisation. npj Comput. Mater. 6, 1–18 (2020).
- [25] Garrity, K. F. & Choudhary, K. Database of Wannier tight-binding Hamiltonians using high-throughput density functional theory. *Sci. Data* 8, 1–10 (2021).
- [26] Qiao, J., Pizzi, G. & Marzari, N. Automated mixing of maximally localized Wannier functions into target manifolds. *npj Comput. Mater.* **9**, 1–9 (2023).
- [27] Qiao, J., Pizzi, G. & Marzari, N. Projectability disentanglement for accurate and automated electronic-structure Hamiltonians. *npj Comput. Mater.* **9**, 1–14 (2023).
- [28] Mounet, N. et al. Two-dimensional materials from high-throughput computational exfoliation of experimentally known compounds. Nat. Nanotechnol. 13, 246–252 (2018).

- [29] Campi, D., Mounet, N., Gibertini, M., Pizzi, G. & Marzari, N. Expansion of the Materials Cloud 2D Database. ACS Nano 17, 11268–11278 (2023).
- [30] Zhang, Y. et al. Different types of spin currents in the comprehensive materials database of nonmagnetic spin Hall effect. npj Comput. Mater. 7, 1–7 (2021).
- [31] Li, H. et al. Intraband and interband spin-orbit torques in noncentrosymmetric ferromagnets.

 Phys. Rev. B 91, 134402 (2015).
- [32] Seemann, M., Ködderitzsch, D., Wimmer, S. & Ebert, H. Symmetry-imposed shape of linear response tensors. *Phys. Rev. B* **92**, 155138 (2015).
- [33] Roy, A., Guimarães, M. H. D. & Sławińska, J. Unconventional spin hall effects in nonmagnetic solids. *Phys. Rev. Mater.* **6**, 045004 (2022).
- [34] Liu, L. et al. Symmetry-dependent field-free switching of perpendicular magnetization. Nat. Nanotechnol. 16, 277–282 (2021).
- [35] Larsen, A. H. et al. The atomic simulation environment—a Python library for working with atoms. J. Phys.: Condens. Matter 29, 273002 (2017).
- [36] Feng, W. et al. Intrinsic spin Hall effect in monolayers of group-VI dichalcogenides: A first-principles study. Phys. Rev. B 86, 165108 (2012).
- [37] Zhou, J., Poncé, S. & Charlier, J.-C. Enhanced spin Hall ratio in two-dimensional semiconductors. *npj Comput. Mater.* **10**, 1–8 (2024).
- [38] Zhou, J., Qiao, J., Bournel, A. & Zhao, W. Intrinsic spin Hall conductivity of the semimetals MoTe₂ and WTe₂. *Phys. Rev. B* **99**, 060408(R) (2019).
- [39] Giustino, F. Electron-phonon interactions from first principles. Rev. Mod. Phys. 89, 015003 (2017).
- [40] Poncé, S., Margine, E. R. & Giustino, F. Towards predictive many-body calculations of phonon-limited carrier mobilities in semiconductors. *Phys. Rev. B* **97**, 121201 (2018).
- [41] Poncé, S., Li, W., Reichardt, S. & Giustino, F. First-principles calculations of charge carrier mobility and conductivity in bulk semiconductors and two-dimensional materials. Rep. Prog. Phys. 83, 036501 (2020).
- [42] Kane, C. L. & Mele, E. J. Quantum Spin Hall Effect in Graphene. Phys. Rev. Lett. 95, 226801 (2005).
- [43] Costa, M. et al. Discovery of higher-order topological insulators using the spin Hall conductivity as a topology signature. npj Comput. Mater. 7, 1–6 (2021).

- [44] Giannozzi, P. et al. Advanced capabilities for materials modelling with Quantum ESPRESSO.
 J. Phys.: Condens. Matter 29, 465901 (2017).
- [45] Huber, S. P. et al. AiiDA 1.0, a scalable computational infrastructure for automated reproducible workflows and data provenance. Sci. Data 7, 1–18 (2020).
- [46] Marzari, N., Vanderbilt, D., De Vita, A. & Payne, M. C. Thermal Contraction and Disordering of the Al(110) Surface. Phys. Rev. Lett. 82, 3296–3299 (1999).
- [47] Sohier, T., Calandra, M. & Mauri, F. Density functional perturbation theory for gated twodimensional heterostructures: Theoretical developments and application to flexural phonons in graphene. Phys. Rev. B 96, 075448 (2017).
- [48] Prandini, G., Marrazzo, A., Castelli, I. E., Mounet, N. & Marzari, N. Precision and efficiency in solid-state pseudopotential calculations. *npj Computational Materials* 4, 72 (2018).
- [49] van Setten, M. J. et al. The PseudoDojo: Training and grading a 85 element optimized norm-conserving pseudopotential table. Comput. Phys. Commun. 226, 39–54 (2018).
- [50] Pseudodojo semicore states. Github (2023). URL https://github.com/aiidateam/aiida-wannier90-workflows/blob/main/src/aiida_wannier90_workflows/utils/pseudo/data/semicore/PseudoDojo_0.4_PBE_FR_standard_upf.json.
- [51] Pizzi, G. et al. Wannier90 as a community code: new features and applications. J. Phys.: Condens. Matter 32, 165902 (2020).
- [52] Poncé, S., Margine, E., Verdi, C. & Giustino, F. Epw: Electron-phonon coupling, transport and superconducting properties using maximally localized wannier functions. *Computer Physics Communications* 209, 116 – 133 (2016).
- [53] Lee, H. et al. Electron-phonon physics from first principles using the EPW code. npj Comput. Mater. 9, 1–26 (2023).
- [54] Zhou, J., Poncé, S. & Charlier, J.-C. Guidelines for accurate and efficient calculations of mobilities in two-dimensional semiconductors. *Phys. Rev. B* **110**, 125304 (2024).
- [55] Poncé, S. et al. First-principles predictions of Hall and drift mobilities in semiconductors. Phys. Rev. Res. 3, 043022 (2021).
- [56] Wu, Q., Zhang, S., Song, H.-F., Troyer, M. & Soluyanov, A. A. WannierTools: An open-source software package for novel topological materials. *Comput. Phys. Commun.* 224, 405–416 (2018).

[57] Zhou, J., Poncé, S. & Charlier, J.-C. Materials Cloud Archive. URL https://archive.materialscloud.org/record/2024.203.

ACKNOWLEDGEMENTS

S. P. acknowledges the support from the Fonds de la Recherche Scientifique de Belgique (F.R.S.-FNRS). J. Z. and J.-C. C. acknowledge financial support from the Fédération Wallonie-Bruxelles through the ARC Grant "DREAMS" (No. 21/26-116), from the EOS project "CONNECT" (No. 40007563), and from the Belgium F.R.S.-FNRS through the research project (No. T.029.22F). Computational resources have been provided by the PRACE/EuroHPC award granting access to MareNostrum5 at Barcelona Supercomputing Center (BSC), Spain and Discoverer at SofiaTech, Bulgaria (OptoSpin project ID. 2020225411), and by the Consortium des Équipements de Calcul Intensif (CÉCI), funded by the F.R.S.-FNRS under Grant No. 2.5020.11 and by the Walloon Region.

AUTHOR CONTRIBUTIONS

J. Z. designed the study and performed calculations. S. P. and J.-C. C. supervised the project. All authors analyzed the results and contributed to writing the paper.

COMPETING INTERESTS

The authors declare no competing interests.

ADDITIONAL INFORMATION

Supplementary information

The supplementary material has been attached.

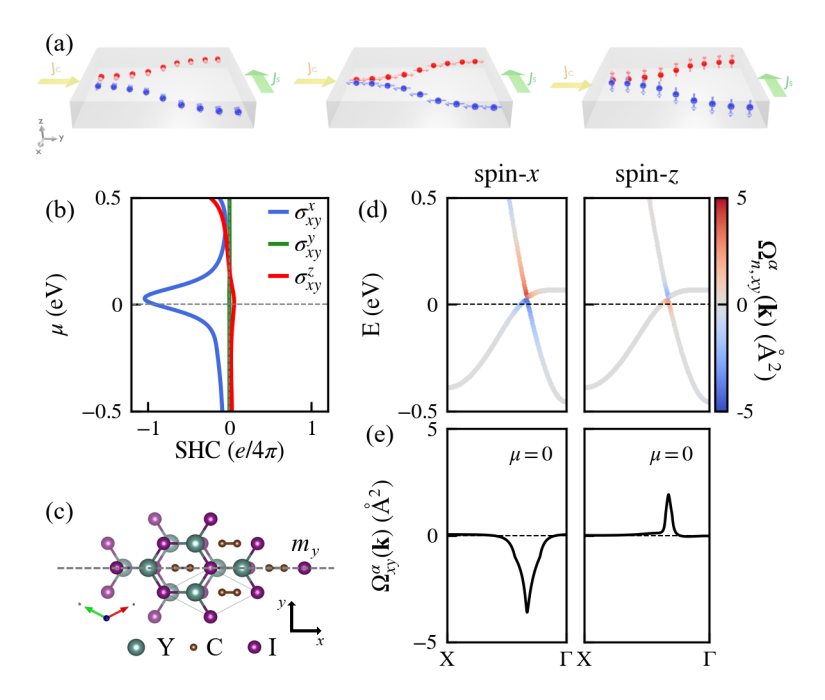


Fig. 1. Canted spin current in $Y_2C_2I_2$. (a) Diagram of spin Hall effect components σ_{xy}^x , σ_{xy}^y , and σ_{xy}^z , respectively. (b) Fermi energy μ -dependent room-temperature spin Hall conductivity components, (c) atomic structure and mirror symmetry, (d) band-resolved spin Berry curvature defined by Eq. (3), and (e) **k**-resolved spin Berry curvature defined by Eq. (2) for $Y_2C_2I_2$ [C2/m] with unconventional spin Hall effect.

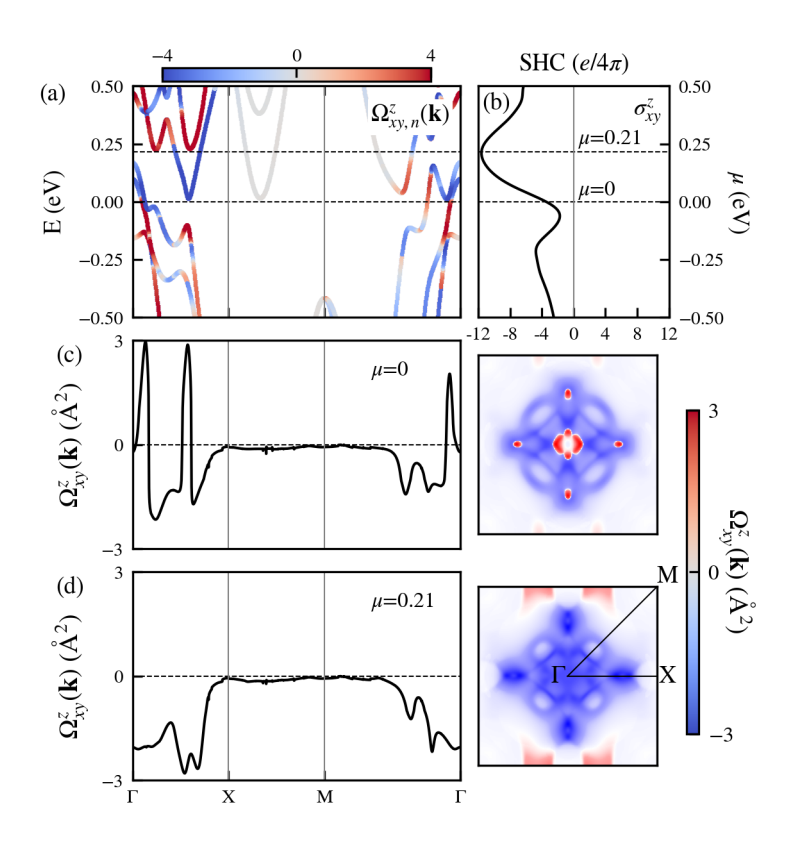


Fig. 2. High spin Hall conductivity in Ta_4Se_2 . (a) Band structure projected by spin Berry curvature, (b) μ -dependent room-temperature spin Hall conductivity σ^z_{xy} , and **k**-resolved spin Berry curvatures respectively for (c) $\mu = 0$ and (d) $\mu = 0.21$ eV of Ta_4Se_2 monolayer.

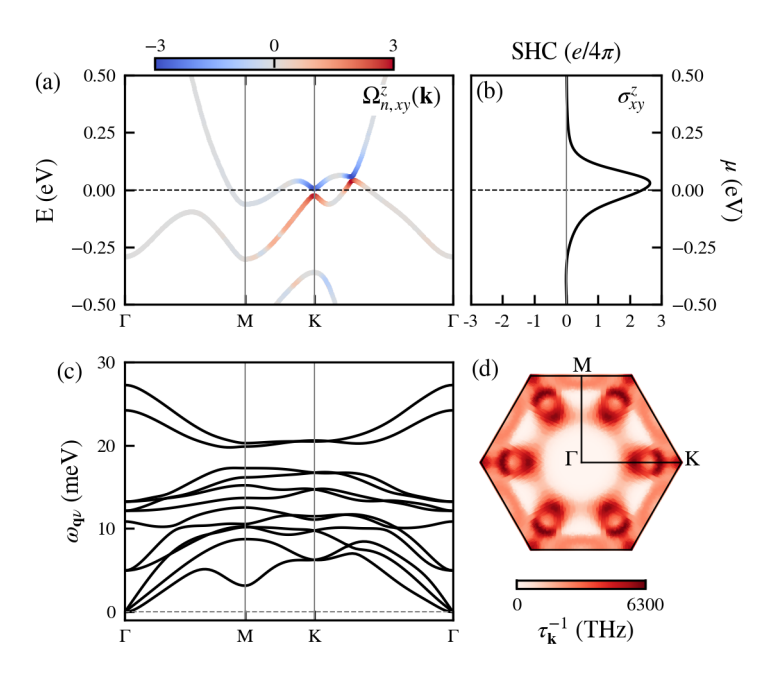


Fig. 3. **High spin Hall ratio in Y**₂**Br**₂. (a) Bands projected by spin Berry curvature, (b) μ -dependent room-temperature spin Hall conductivity σ_{xy}^z , (c) phonon dispersion, and (d) **k**-resolved electron-phonon scattering rate of Y₂Br₂.

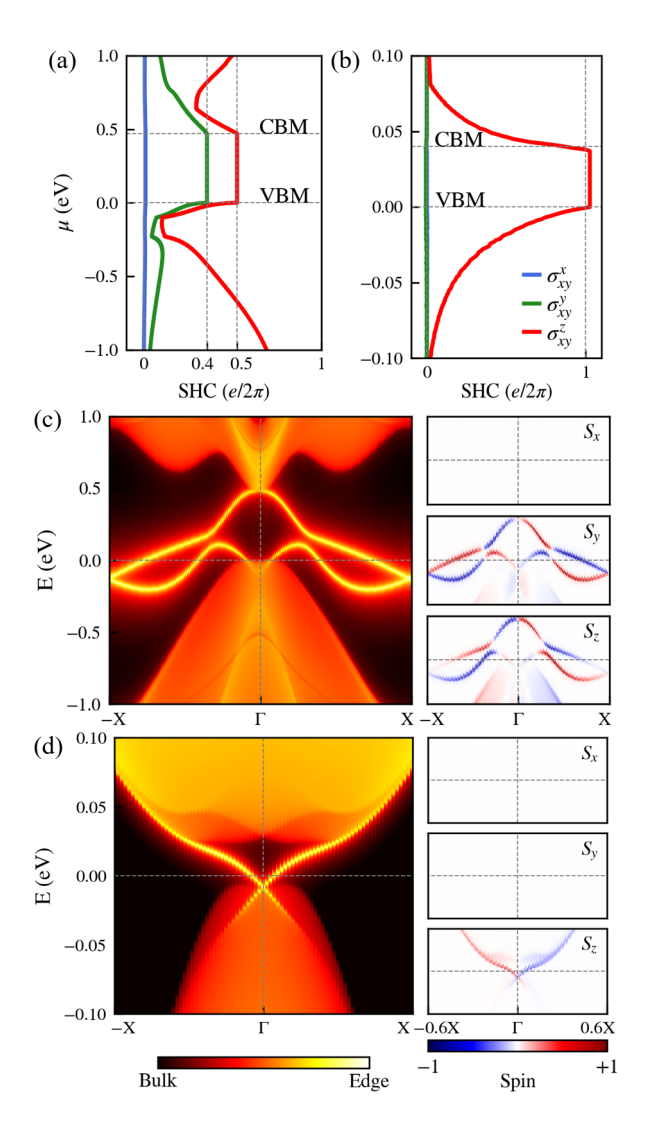


Fig. 4. Spin Hall conductivities and edge states in quantum spin Hall insulators. μ -dependent spin Hall conductivity components of (a) Bi₂ and (b) CuLi₂As at T=0 K. Edge states and spin projections of (c) Bi₂ and (d) CuLi₂As. The conduction band minimum is abbreviated as CBM, valence band maximum is abbreviated as VBM.

Table 1. Stable metals with high conventional spin Hall conductivity σ_{xy}^z .

Material	Space group	$\sigma_{xy}^z \ (e/4\pi)$
Ta_4Se_2	P4/nmm	-3.4
$\mathrm{Sn_2P}$	P1	-2.7
Y_2Br_2	P-3m1	2.4

Table 2. List of quantum spin Hall insulators. SG is the abbreviation of space group, σ_{xy}^z denotes the plateau value in band gap, and S_z illustrates whether the out-of-plane spin is conserved or not.

Monolayer	$E_{\rm gap}~({\rm meV})$	SG	$\sigma_{xy}^z \ (e/2\pi)$	S_z
Bi_2	471	P-3m1	0.5	no
$\mathrm{Hf_2Br_2}$	69	P-3m1	-0.9	no
$CuLi_2As$	41	P-6m2	1.0	yes
$\mathrm{Ti}_{2}\mathrm{N}_{2}\mathrm{I}_{2}$	19	Pmmn	-1.0	yes